CrystEngComm

Accepted Manuscript

ROYAL SOCIETY OF CHEMISTRY

www.rsc.org/crystengcomm

TEM study on $HgIn_2Te_4$ precipitates in $Hg_3In_2Te_6$ crystals grown by Bridgman method

Lin Luo, Wanqi Jie*, Yadong Xu, Yihui He, Lingyan Xu, Li Fu

State Key Laboratory of Solidification Processing, School of Materials Science and Engineering, Northwestern Polytechnical University, Xi'an 710072, China

Abstract:

Transmission electron microscopy (TEM) is used to investigate precipitates in $Hg_3In_2Te_6$ crystals grown by Bridgman method. The results show that small volume fractions of $HgIn_2Te_4$ and $Hg_5In_2Te_8$ coexist in the crystals, which indicates a small portion of $Hg_3In_2Te_6$ crystals has been decomposed. $HgIn_2Te_4$ precipitates contain three types of equivalent variants with the preferred growth directions along <100> family of crystal directions of $Hg_3In_2Te_6$ matrix. Furthermore, $HgIn_2Te_4$ precipitates are coherent with $Hg_3In_2Te_6$ matrix.

Keywords: $Hg_3In_2Te_6$; $HgIn_2Te_4$; coherent interface; TEM

* Corresponding author at: 127 Youyi Xilu, Xi'an 710072, China. Tel.: +862988486065; fax: +862988495414. E-mail address:jwq@nwpu.edu.cn

1. Introduction

Ternary compound semiconductor $Hg_3In_2Te_6$ is regarded as a promising novel photoelectric compound for fiber-optic communication [1, 2]. The detectors used in fiber-optic communication should have fast response speeds, which demand that $Hg_3In_2Te_6$ crystals possess high carrier mobility. At present, the carrier mobility of $Hg_3In_2Te_6$ crystals grown by Bridgman method is as low as 4.60×10^2 $cm^2V^{-1}s^{-1}$ [3], which hinders its practical application. Precipitates are considered to have important effect on carrier mobility in semiconductors [4, 5]. Moreover, precipitates, as trapping centers, influence the signal collection of detectors [6, 7]. The presence of precipitates is difficult to avoid during crystal growth process. Thus, in order to improve the crystal property by controlling the species, densities and distributions of precipitates, it is meaningful to make an insight on the characteristic of precipitates. To date, the study on $Hg_3In_2Te_6$ crystals mainly focus on physical properties [2, 8, 9] and device performances[1, 10, 11], but seldom on the precipitates.

$Hg_3In_2Te_6$ crystallizes into the defect zinc-blende phase at high temperature, in which one-sixth of the cation sublattice sites are occupied randomly by structural vacancies [12]. Grushka [13] and Leute [14] reported that $Hg_3In_2Te_6$ decomposed into two phases $Hg_5In_2Te_8$ and $HgIn_2Te_4$ at 585K or slightly higher temperature, i.e., $2Hg_3In_2Te_6 = Hg_5In_2Te_8 + HgIn_2Te_4$. But Maynell [15] considered that an order–disorder transformation happens at 585K. In In_2Te_3-Hg_3Te_3 system, $Hg_3In_2Te_6$, $Hg_5In_2Te_8$ and $HgIn_2Te_4$, corresponding to the composition x = 0.5, 0.375 and 0.75, are defined as α_2, β and γ phase, respectively[16]. If the above decomposition reaction occurs, $HgIn_2Te_4$ and $Hg_5In_2Te_8$ should coexist in samples. The presence of $Hg_5In_2Te_8$ precipitates in $Hg_3In_2Te_6$ crystals grown by Bridgman method has been reported [17].

This work tries to find the coexistence of $HgIn_2Te_4$ and $Hg_5In_2Te_8$ precipitates in $Hg_3In_2Te_6$

crystals grown by Bridgman method for confirming the decomposition reaction. Besides, the orientation relationship and the interface structure between $HgIn_2Te_4$ precipitates and $Hg_3In_2Te_6$ matrix are discussed.

2. Material and methods

All $Hg_3In_2Te_6$ samples used in the work came from ingots grown by vertical Bridgman method in the State Key Laboratory of Solidification Processing (SKLSP) in China. The growth procedure was described in detail elsewhere [9]. For TEM samples, $Hg_3In_2Te_6$ wafers were mechanically ground to a thickness of 40 μm, and then thinned using Gatan 691 ion beam thinner to obtain electron transparent thin areas. Small angle, low voltage and liquid nitrogen cooling were used to avoid the artifacts during milling. Selected area electron diffraction (SAED) and high-resolution transmission electron microscopy (HRTEM) were performed using a Tecnai F30 G^2 electron microscope with the incident electron energy of 300 keV. Generally, zone axes and crystal directions appeared in the paper are corresponding to the structure of $Hg_3In_2Te_6$ matrix. A small portion of the samples were cleaned and finely ground into powders for X-ray diffraction (XRD) analysis. XRD data were collected using a X'Pert MPO Pro X-ray diffractometer with the wavelength of 0.15406 nm ($Cu_{K\alpha}$). The accelerating voltage and current were 40 kV and 35 mA, respectively.

3. Results and discussion

3.1 Existence of $HgIn_2Te_4$ precipitates

Fig. 1 is a SAED pattern observed in a few areas of $Hg_3In_2Te_6$ samples. The set of diffraction

spots with strong intensity is indexed as the fundamental reflections corresponding to the $Hg_3In_2Te_6$ phase with disordered vacancies along $[110]_m$ zone axis. The subscript m represents $Hg_3In_2Te_6$ matrix. The PDF number, space group and lattice constant a_m of the zinc-blende phase (α_2 phase) are 65-5765, $F\bar{4}3m$ (216) and 0.6298 nm, respectively. The weak set is indexed as the reflections of $Hg_5In_2Te_8$ phase (β phase) along $[110]_\beta$ zone axis. β phase is also belong to zinc-blende structure. Its space group and lattice constant a_β are $F\bar{4}3m$ (216) and 1.26723 nm, respectively [17-18].

Nevertheless, a different SAED pattern was found along the same zone axis, as shown in Fig. 2a. The set of diffraction spots with strong intensity is still corresponding to the reflections of α_2 phase. In comparison with Fig. 1, the weak set exists only at the midpoints between two neighboring strong spots along [002] and $[2\bar{2}0]$ and no weak diffraction spot exists between two neighboring strong spots along $[1\bar{1}\bar{1}]$ and $[1\bar{1}1]$. The weak set is consistent with the reflections of $HgIn_2Te_4$ phase (γ phase) along $[110]_\gamma$ zone axis. γ phase is belong to body-centered tetragonal structure. Its PDF number, space group, lattice constants a_γ and c_γ are 74-0220, $I\bar{4}$ (82), 0.6186 nm and 1.237 nm, respectively. Fig. 2b is the dark-field micrograph corresponding to the weak diffraction spot $[001]_m$ in Fig. 2a. The precipitates exhibit rod-shaped morphologies and their growth directions are close to $[001]_m$.

In order to further confirm the presence of γ phase, the zone axis of Fig. 2a was rotated to $[111]_m$ and a SAED pattern was obtained, as shown in Fig. 3a. The set of diffraction spots with strong intensity is indexed as the reflections of α_2 phase along $[111]_m$ zone axis. The weak diffraction spots exist at the midpoints between two neighboring strong spots along $[2\bar{2}0]_m$, $[20\bar{2}]_m$ and $[02\bar{2}]_m$. Furthermore, the weak diffraction spots have different intensities along

different <220>$_m$ directions. Specifically, the weak spot (V3) along $[20\bar{2}]_m$ has the highest intensity and the weak spot (V2) along $[2\bar{2}0]_m$ has the lowest intensity. Hence, the weak diffraction spots in Fig. 3a may be composed of three sets of diffraction spots.

To confirm the above conclusion, HRTEM images were recorded, as shown in Fig. 3b~d. The HRTEM images and the SAED pattern come from the same area. Three precipitates V1~3 can be found and their growth directions are $[2\bar{1}\bar{1}]_m$, $[11\bar{2}]_m$ and $[1\bar{2}1]_m$, respectively. The growth directions have a rotation relationship of 120° with each other. Fig. 3e~h are the fast Fourier transform (FFT) patterns of the matrix and V1~3, respectively. The superimposition of the FFT patterns of V1~3 can yield the same pattern as the SAED pattern in Fig. 3a. Meanwhile, the three FFT patterns can coincide with each other, when the patterns are rotated by 120° along $[111]_m$ zone axis, which implies that the three FFT patterns are equivalent. In addition, the three FFT patterns can be indexed as the reflections of γ phase along <221>$_\gamma$ zone axes, respectively. To sum up, the SAED pattern in Fig. 3a are created by three variants of γ phase. It should be stressed that the three FFT patterns can also be indexed as the reflections of β phase along <111>$_\beta$ zone axes, respectively. However, Fig. 3a was produced through the rotation of Fig. 2a, so the three FFT patterns are corresponding to γ phase.

Sometimes, only two variants (V1+V3) were displayed and another variant V2 was not displayed in the SAED pattern along $[111]_m$ zone axis, as shown in Fig. 4. The possible reason is that the volume of V2 in the field of vision of SAED is small and the intensity of the corresponding diffraction spot is very weak. Moreover, V1 and V3 have different intensities. Fig. 4 confirms that the SAED pattern in Fig. 3a come from the three variants of γ phase.

Thus, $HgIn_2Te_4$ precipitates exist in $Hg_3In_2Te_6$ crystals grown by Bridgman method, except

for $Hg_5In_2Te_8$ precipitates. As shown in Fig. 5, all diffraction peaks in the powder XRD pattern of the samples are corresponding to $Hg_3In_2Te_6$ matrix (PDF number: 65-5765) and no extra peak is found. Thereby, the volume fractions of $HgIn_2Te_4$ and $Hg_5In_2Te_8$ precipitates are less than the detection limit 5% in powder XRD measurements.

3.2 The orientation relationship between $HgIn_2Te_4$ precipitates and $Hg_3In_2Te_6$ matrix

The projections of [001] direction along [110] and [111] zone axes are [001] and $[11\bar{2}]$, which agree with the growth directions of the variant in Fig. 2b and 3c, respectively. Therefore, it is expected that c axes of the three variants of γ phase are parallel to [001], [100] and [010] directions of $Hg_3In_2Te_6$ matrix, respectively, as shown in Fig. 6. Tab. 1 is equivalent orientations in space between the matrix and the three variants of γ phase, which is calculated based on Fig. 6.

Tab. 1 shows that $[111]_m$ in the matrix is parallel to $[221]_1$ in V1, $[2\bar{2}1]_2$ in V2 and $[22\bar{1}]_3$ in V3, respectively. The subscripts 1~3 represent the variants V1~3. Fig. 3i~k are simulated electron diffraction patterns of V1~3 in Fig. 6 along $[221]_1$, $[2\bar{2}1]_2$ and $[22\bar{1}]_3$ zone axes, respectively. The annotations in Fig. 3i~k are corresponding to V1~3, respectively. Blue circles were drawn to show the correspondence between Fig. 3i~k. It can be found that the patterns in Fig. 3i~k are consistent with the FFT patterns in Fig. 3f~h, respectively. Furthermore, the superimposition of the patterns in Fig. 3i~k is consistent with the SAED pattern in Fig. 3a.

Fig. 7a is a SAED pattern along $[110]_m$ zone axis. Fig. 7b~d are simulated electron diffraction patterns of V1~3 along $[110]_1$, $[0\bar{2}1]_2$ and $[201]_3$ zone axes, which are parallel to $[110]_m$, respectively. Fig. 8a is a SAED pattern along $[\bar{3}\bar{2}1]_m$ zone axis. Fig. 8b~d are simulated electron diffraction patterns of V1~3 along $[\bar{6}\bar{4}1]_1$, $[\bar{2}4\bar{3}]_2$ and $[\bar{3}1\bar{1}]_3$ zone axes, which are parallel to $[\bar{3}\bar{2}1]_m$, respectively. It can be found that the SAED patterns in Fig. 7a and 8a are consistent

with the superimpositions of the simulated patterns in Fig. 7b~d and 8b~d, respectively.

To sum up, Fig. 3i~k and Fig. 7~8 confirm that the c axes of the three variants of γ phase are parallel to <001> directions of $Hg_3In_2Te_6$ matrix. Thereby, the preferred growth directions of the three variants are [001], [100] and [010] of $Hg_3In_2Te_6$ matrix, respectively. Similar orientation relationship can be observed between $Hg_5In_2Te_8$ precipitates and $Hg_3In_2Te_6$ matrix [17]. The structures of $HgIn_2Te_4$ and $Hg_3In_2Te_6$ decide that their interface energy will reach the minimum, only when the above orientation relationship is established. This can be explained as follows. $HgIn_2Te_4$ (γ phase) is belong to body-centered tetragonal structure. Its lattice constants $a_\gamma = b_\gamma =$ 0.6186 nm = $0.982a_m \approx a_m$, $c_\gamma =$ 1.237 nm = $1.964a_m \approx 2a_m$. It is well known that the coherent interface has the lowest interface energy. For $HgIn_2Te_4$ and $Hg_3In_2Te_6$, the coherent interface can form, only when c_γ axis is parallel to [001], [100] or [010] axes of $Hg_3In_2Te_6$.

The coincident site lattice (CSL) calculation was carried out to confirm the above conclusion. We choose the interface between V1 and $Hg_3In_2Te_6$ matrix as an example to describe the calculation. To simplify the calculation, we consider $a_\gamma = b_\gamma = a_m$, $c_\gamma = 2a_m$. For $Hg_3In_2Te_6$, the viewing direction and the rotation axis are $[100]_m$ direction. For V1, the viewing direction is $[100]_1$ direction. As shown in Fig. 9, the $Hg_3In_2Te_6$ and V1 have a coincident site A, after the $Hg_3In_2Te_6$ lattice is rotated by θ angle. Meanwhile, another coincident site B exists on the perpendicular direction of the vector ***OA***. We choose the vectors ***OA*** and ***OB*** as basic vectors to build a CSL. Accordingly, the density Σ of the CSL can be acquired:

$$\Sigma = \frac{|\boldsymbol{OA}||\boldsymbol{OB}|}{|\boldsymbol{R}_{bm}||\boldsymbol{R}_{cm}|} \quad (1)$$

When Σ reaches the lowest value, the interface energy is the lowest. The expression of Σ can be obtained through the following calculation. After the rotation, the basic vectors $\boldsymbol{R}_{\mathrm{bm}}$ and $\boldsymbol{R}_{\mathrm{cm}}$ of $Hg_3In_2Te_6$ matrix are changed to $\boldsymbol{R}'_{\mathrm{bm}}$ and $\boldsymbol{R}'_{\mathrm{cm}}$, the vector $\boldsymbol{OA}$ can be written as:

$$\boldsymbol{OA} = m_A \boldsymbol{R}'_{bm} + n_A \boldsymbol{R}'_{cm} \tag{2}$$

Their modules are as follows:

$$\left|\boldsymbol{R}'_{\mathrm{bm}}\right| = \left|\boldsymbol{R}'_{\mathrm{cm}}\right| = \left|\boldsymbol{R}_{\mathrm{bm}}\right| = \left|\boldsymbol{R}_{\mathrm{cm}}\right| = \mathrm{a_m} \tag{3}$$

$$\left|\boldsymbol{OA}\right| = \sqrt{(m_A \left|\boldsymbol{R}'_{bm}\right|)^2 + (n_A \left|\boldsymbol{R}'_{cm}\right|)^2} \tag{4}$$

Therefore,

$$\left|\boldsymbol{OA}\right| = a_m \sqrt{m_A^2 + n_A^2} \tag{5}$$

For V1,

$$\boldsymbol{OA} = p_{\mathrm{A}} \boldsymbol{R}_{\mathrm{b}\gamma} + q_{\mathrm{A}} \boldsymbol{R}_{\mathrm{c}\gamma} \tag{6}$$

$$\left|\boldsymbol{OA}\right| = \sqrt{(p_A \left|\boldsymbol{R}_{b\gamma}\right|)^2 + (q_A \left|\boldsymbol{R}_{c\boldsymbol{\gamma}}\right|)^2} \tag{7}$$

$$\left|\boldsymbol{R}_{b\gamma}\right| = b_\gamma = a_m \tag{8}$$

$$\left|\boldsymbol{R}_{c\gamma}\right| = c_\gamma = 2a_m \tag{9}$$

Thus,

$$\left|\boldsymbol{OA}\right| = a_m \sqrt{p_A^2 + 4q_A^2} \tag{10}$$

The following equation can be obtained through combining the equations R-5 and R-10:

$$p_{\mathrm{A}}^2 + 4q_{\mathrm{A}}^2 = m_{\mathrm{A}}^2 + n_{\mathrm{A}}^2 \tag{11}$$

Similarly, for the vector $\boldsymbol{OB}$,

$$\left|\boldsymbol{OB}\right| = a_m \sqrt{p_{\boldsymbol{B}}^2 + 4q_B^2} \tag{12}$$

$$p_{\mathrm{B}}^2 + 4q_B^2 = m_{\mathrm{B}}^2 + n_{\mathrm{B}}^2 \tag{13}$$

After substituting the equations R-3, R-10 and R-12 in the equation R-1, Σ can be written as:

$$\Sigma = \sqrt{p_A^2 + 4q_{\mathrm{A}}^2} \sqrt{p_B^2 + 4q_{\mathrm{B}}^2} \tag{14}$$

Here, p_{A}, p_{B}, q_{A} and q_{B} are integers. The equations $p_{\mathrm{A}} = p_{\mathrm{B}}$ and $q_{\mathrm{A}} = q_{\mathrm{B}}$ cannot be simultaneously true, since the vector $\boldsymbol{OA}$ is perpendicular to the vector $\boldsymbol{OB}$. Meanwhile, the

existence of the vector ***OA*** requires that p_A and q_A cannot be simultaneously zero. Similarly, p_B and q_B cannot be simultaneously zero. Hence, Σ will reach the lowest value, only when (1) $p_A = 0$, $q_A = 1$, $p_B = 1$ and $q_B = 0$ or (2) $p_A = 1$, $q_A = 0$, $p_B = 0$ and $q_B = 1$. In this case, Σ = 2 and θ = 0 or ±90°. It can be found that θ = 0 is corresponding to V1 and θ = ±90° are corresponding to V3. The relationship between V2 and $Hg_3In_2Te_6$ matrix can also be confirmed by a similar calculation.

3.3 Interface between $HgIn_2Te_4$ precipitates and $Hg_3In_2Te_6$ matrix

Fig. 10a and 10b are the HRTEM image of $HgIn_2Te_4$ variant 1 (V1) and the corresponding FFT pattern, respectively. The FFT pattern is indexed as the reflections corresponding to V1 along $[110]_1$ zone axis. In Fig. 10a, $HgIn_2Te_4$ variant 1 has two domains (1 and 2). In comparison with $Hg_3In_2Te_6$ matrix, the two domains have double periodicities along [001]. The growth directions of the two domains are [001], which is the same as the growth directions of $HgIn_2Te_4$ precipitates in Fig. 2b. Meanwhile, the two domains have a displacement of $c_\gamma/2 \approx c_m$ along [001] and an antiphase boundary (APB). The displacement and the APB are masked by blue lines and a white line, respectively. Furthermore, the transition from the matrix to the domains is smooth. In order to show the point clearly, we drew the intensity profiles of the dots along straight lines c and d, as shown in Fig. 10c and 10d. The peak values of the intensity of the dots change slowly along the lines and no sudden change exists. Besides, the interface between the two domains and $Hg_3In_2Te_6$ matrix are coherent and no interface dislocations can be found. Similar results can be observed in the interface between $Hg_5In_2Te_8$ precipitates and $Hg_3In_2Te_6$ matrix [17]. Based on interface theory [19], the presence of coherent interface suggests that their lattice mismatch along [001] is lower than 5%, which agrees with the theoretical lattice mismatch $(2c_m-c_\gamma)/c_\gamma = (2\times6.298-12.37)/12.37 = 1.8\%$.

To sum up, the growth process of γ phase is as follows. First of all, a few γ phase nuclei form. Furthermore, the nuclei grow preferably at relatively high speed along <100>. At the same time, the nuclei grow at relatively low speed along the other directions. Finally, a few nuclei, which grow along the same <100> directions, contact each other and form a big precipitate. An APB will form, if two contact nuclei have a displacement along the interface.

4. Conclusions

Precipitates in $Hg_3In_2Te_6$ crystals grown by Bridgman method are studied by TEM. The results show that the crystals contain $HgIn_2Te_4$ and $Hg_5In_2Te_8$ precipitates, indicating a small portion of $Hg_3In_2Te_6$ crystals has been decomposed. $HgIn_2Te_4$ precipitates exhibit rod-shaped morphologies and contain three equivalent variants with the preferred growth directions along <100> family of crystal directions of $Hg_3In_2Te_6$ matrix. Furthermore, the transition from $Hg_3In_2Te_6$ matrix to $HgIn_2Te_4$ precipitates is smooth and their interface are coherent. Antiphase boundaries exist between some $HgIn_2Te_4$ precipitates.

Acknowledgements

The authors thank beneficial discussion and valuable advice with Dr. Maohua Li and Sheng Ouyang. This work has been financially supported by the National "973" Program (2011CB610406), the National Natural Science Foundation of China (Grant No. 51202197, 51172185), the 111 Project of China (Grant No. B08040). It is also supported by the Specialized Research Fund for the Doctoral Program of Higher Education of China (20116102120014), the Natural Science Basic Research Plan in Shaanxi Province of China and the Fund of Ministry of

Education for Doctor (20116102110013).

Reference

1. L. A. Kosyachenko, I. S. Kabanova, V. M. Sklyarchuk, O. F. Sklyarchuk and I. M. Rarenko, *Phys. Status Solidi A*, 2009, 206, 351-355.
2. O. L. Maslyanchuk, L. A. Kosyachenko, German, II, I. M. Rarenko, V. A. Gnatyuk and T. Aoki, *Phys. Status Solidi C* 2009, 6, 1154-1157.
3. L. G. Wang, Y. C. Dong and W. Q. He, *Mater. Res. Bull.*, 2007, 42, 1949-1954.
4. L. R. Weisberg, *J. Appl. Phys.* , 2004, 33, 1817-1821.
5. G. Q. Li, S. J. Shih, S. C. Mu, Y. D. Xu and W. Q. Jie, *J. Mater. Res.* , 2010, 25, 1298-1303.
6. A. E. Bolotnikov, G. S. Camarda, G. A. Carini, Y. Cui, L. Li and R. B. James, *Nuclear Instruments and Methods in Physics Research Section A: Accelerators, Spectrometers, Detectors and Associated Equipment*, 2007, 571, 687-698.
7. G. Carini, A. Bolotnikov, G. Camarda, G. Wright, R. James and L. Li, *Appl. Phys. Lett.* , 2006, 88, 143515.
8. O. G. Grushka, S. M. Chupyra, O. M. Mysliuk, S. V. Bilichuk and D. P. Koziarskyi, *Semiconductors*, 2013, 47, 1141-1144.
9. L. H. Wang, Y. C. Dong and W. Q. Jie, *J. Phys. D-Appl. Phys.*, 2007, 40, 3921-3924.
10. Z. M. Grushka, P. N. Gorley, O. G. Grushka, P. P. Horley, Y. I. Radevych and Z. Zhuo, in *Ico20: Materials and Nanostructures*, eds. W. Lu and J. Young, Spie-Int Soc Optical Engineering, Bellingham, 2006, vol. 6029, pp. A291-A291.
11. L. A. Kosyachenko, Y. S. Paranchich, V. N. Makogonenko, V. M. Sklyarchuk, E. F. Sklyarchuk and German, II, *Tech. Phys.* , 2003, 48, 647-650.
12. A. I. Malik, M. Vieira, M. Fernandes, F. Macarico and Z. M. Grushka, *SPIE*, 1999, 3629, 433-442.
13. G. Grushka, E. Skulish and Z. Grushka, *Izv. Akad. Nauk SSSR, Neorg. Mater.*, 1982, 18, 1388-1390.
14. V. Leute and H. M. Schmidtke, *J. Phys. Chem. Solids* 1988, 49, 409-420.
15. C. A. Maynell, G. A. Saunders and T. Seddon, *Phys. Lett.*, 1970, 23, 338-339.
16. P. Spencer and B. Ray, *J. Phys. D: Appl. Phys.* , 1968, 1, 299-301.
17. J. Sun, L. Fu, H. Liu, Y. Li, S. P. Ringer and Z. Liu, *J. Alloys Compd.* , 2014, 601, 298-306
18. V. R. Kozer, A. O. Fedorchuk, I. D. Olekseyuk and O. V. Parasyuk, *J. Alloys Compd.* , 2010, 503, 40-43.
19. J. Pan, J. Tong and M. Tian, *Foundation of Material Science*, Tsinghua University Press, Bejing, 2011.

Figure captions

Fig. 1 SAED pattern of $Hg_5In_2Te_8$ precipitates along $[110]_m$ zone axis.

Fig.2 SAED pattern and dark-field micrograph of $HgIn_2Te_4$ precipitates along $[110]_m$ zone axis: (a) SAED pattern; (b) dark-field micrograph. The micrograph has been rotated based on magnetic dip.

Fig. 3 SAED pattern, HRTEM images, FFT patterns and simulated electron diffraction patterns of $HgIn_2Te_4$ variants V1~3 along $[111]_m$ zone axis: (a) SAED pattern; (b)~(d) HRTEM images of the three variants; (e) FFT pattern of the matrix; (f)~(h) FFT patterns of the three variants; (i) simulated pattern of V1 along $[221]_1$; (j) simulated pattern of V2 along $[2\bar{2}1]_2$; (k) simulated pattern of V3 along $[22\bar{1}]_3$.

Fig. 4 SAED pattern of $HgIn_2Te_4$. Two variants (V1+V3) were displayed and another variant V2 was not displayed.

Fig. 5 Typical powder XRD pattern of $Hg_3In_2Te_6$ samples measured at room temperature.

Fig. 6 Orientation relationship between $Hg_3In_2Te_6$ matrix and $HgIn_2Te_4$ variants 1~3: (a) $Hg_3In_2Te_6$ matrix; (b)~(d) $HgIn_2Te_4$ variants 1~3.

Fig. 7 SAED pattern and simulated electron diffraction patterns of V1~3: (a) SAED pattern along $[110]_m$ zone axis; (b) simulated pattern of V1 along $[110]_1$; (c) simulated pattern of V2 along $[0\bar{2}1]_2$; (d) simulated pattern of V3 along $[201]_3$.

Fig. 8 SAED pattern and simulated electron diffraction patterns of V1~3: (a) SAED pattern along $[\bar{3}\bar{2}\bar{1}]_m$ zone axis; (b) simulated pattern of V1 along $[\bar{6}\bar{4}\bar{1}]_1$; (c) simulated pattern of V2 along $[\bar{2}4\bar{3}]_2$; (d) simulated pattern of V3 along $[\bar{3}1\bar{1}]_3$.

Fig. 9 A coincident site lattice composed of V1 and $Hg_3In_2Te_6$ matrix. ***OA*** and ***OB*** are basic vectors of the coincident site lattice.

Fig. 10 HRTEM image and the results of $HgIn_2Te_4$ variant 1: (a) HRTEM image; (b) FFT image; (c) and (d) the intensity profiles of the dots along straight lines c and d.

Tab.1 Equivalent crystal orientations between $Hg_3In_2Te_6$ matrix and $HgIn_2Te_4$ variants 1~3.

Structure	Equivalent crystal orientations in space		
$Hg_3In_2Te_6$ matrix	[111]	[110]	$[\bar{3}\bar{2}\bar{1}]$
$HgIn_2Te_4$ variant 1 (V1)	[221]	[110]	$[\bar{6}\bar{4}\bar{1}]$
$HgIn_2Te_4$ variant 2 (V2)	$[2\bar{2}1]$	$[0\bar{2}1]$	$[\bar{2}4\bar{3}]$
$HgIn_2Te_4$ variant 3 (V3)	$[22\bar{1}]$	[201]	$[\bar{3}1\bar{1}]$

A table of contents entry

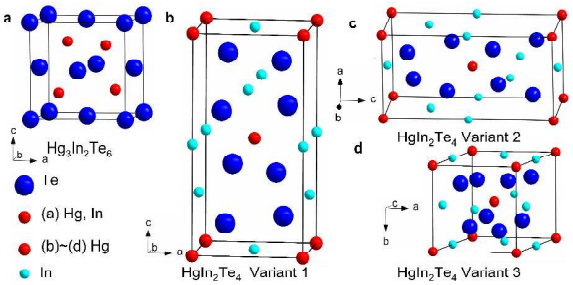

$HgIn_2Te_4$ precipitates, which coexist with $Hg_5In_2Te_8$ in $Hg_3In_2Te_6$ crystals, have three variants with the $<100>_m$ growth directions of $Hg_3In_2Te_6$ crystals.

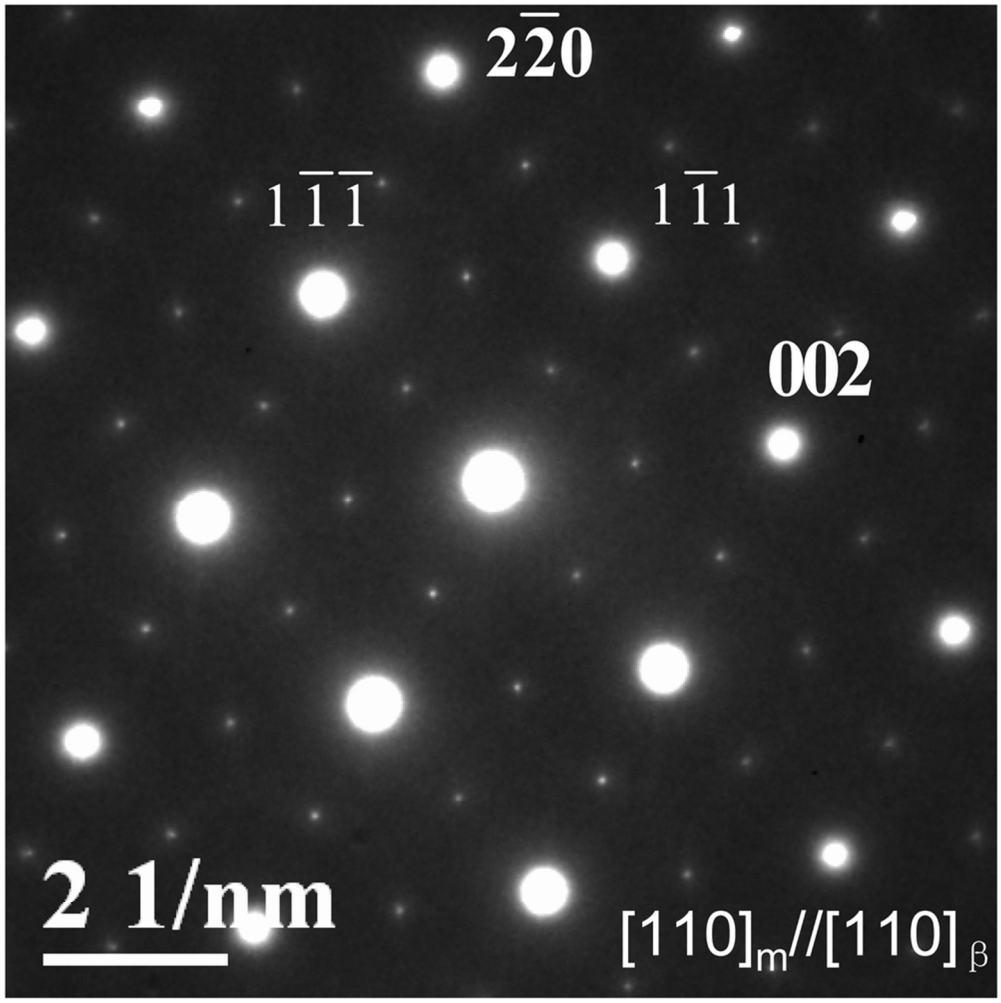

Fig. 1 SAED pattern of $Hg_5In_2Te_8$ precipitates along [110]m zone axis.
85x85mm (300 x 300 DPI)

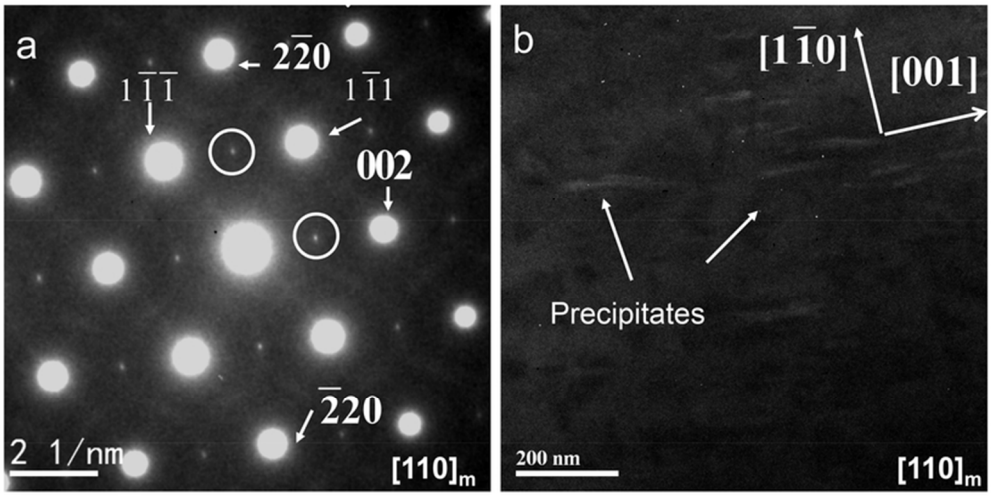

Fig.2 SAED pattern and dark-field micrograph of $HgIn_2Te_4$ precipitates along $[110]_m$ zone axis: (a) SAED pattern; (b) dark-field micrograph. The micrograph has been rotated based on magnetic dip.
69x34mm (300 x 300 DPI)

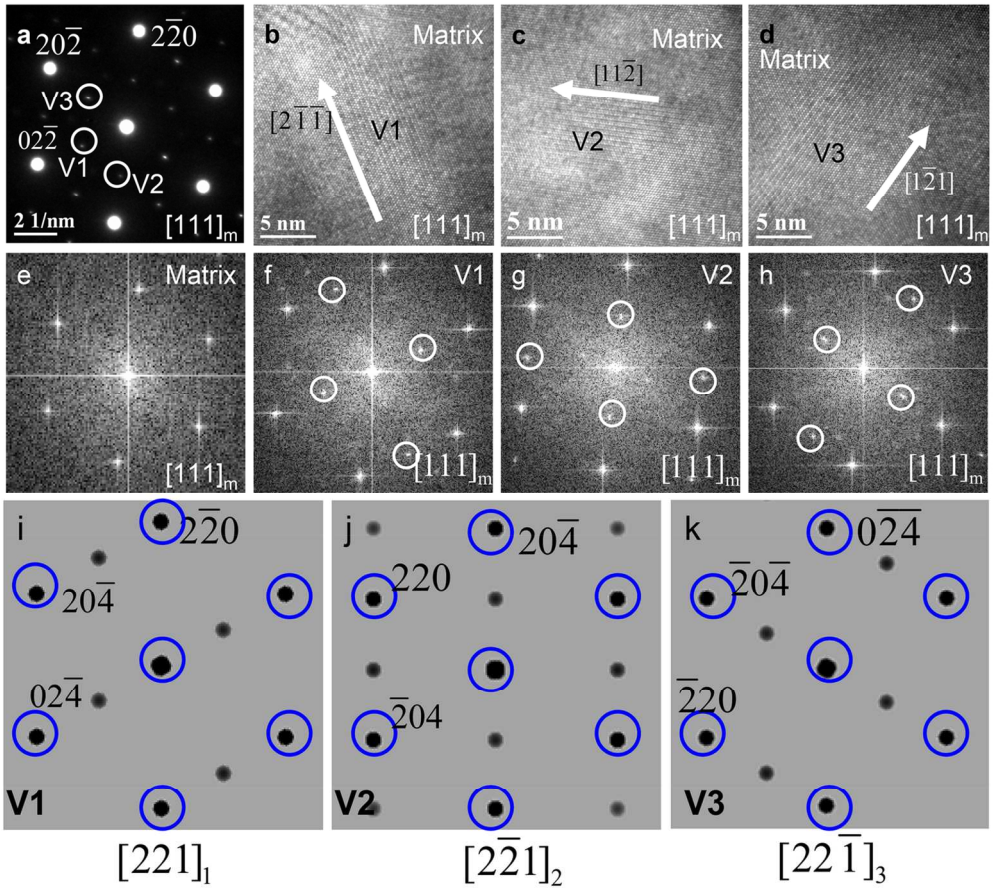

Fig. 3 SAED pattern, HRTEM images, FFT patterns and simulated electron diffraction patterns of $HgIn_2Te_4$ variants V1~3 along $[111]_m$ zone axis: (a) SAED pattern; (b)~(d) HRTEM images of the three variants; (e) FFT pattern of the matrix; (f)~(h) FFT patterns of the three variants; (i) simulated pattern of V1 along $[221]_1$; (j) simulated pattern of V2 along $[2\text{-}21]_2$; (k) simulated pattern of V3 along $[22\text{-}1]_3$.
124x110mm (300 x 300 DPI)

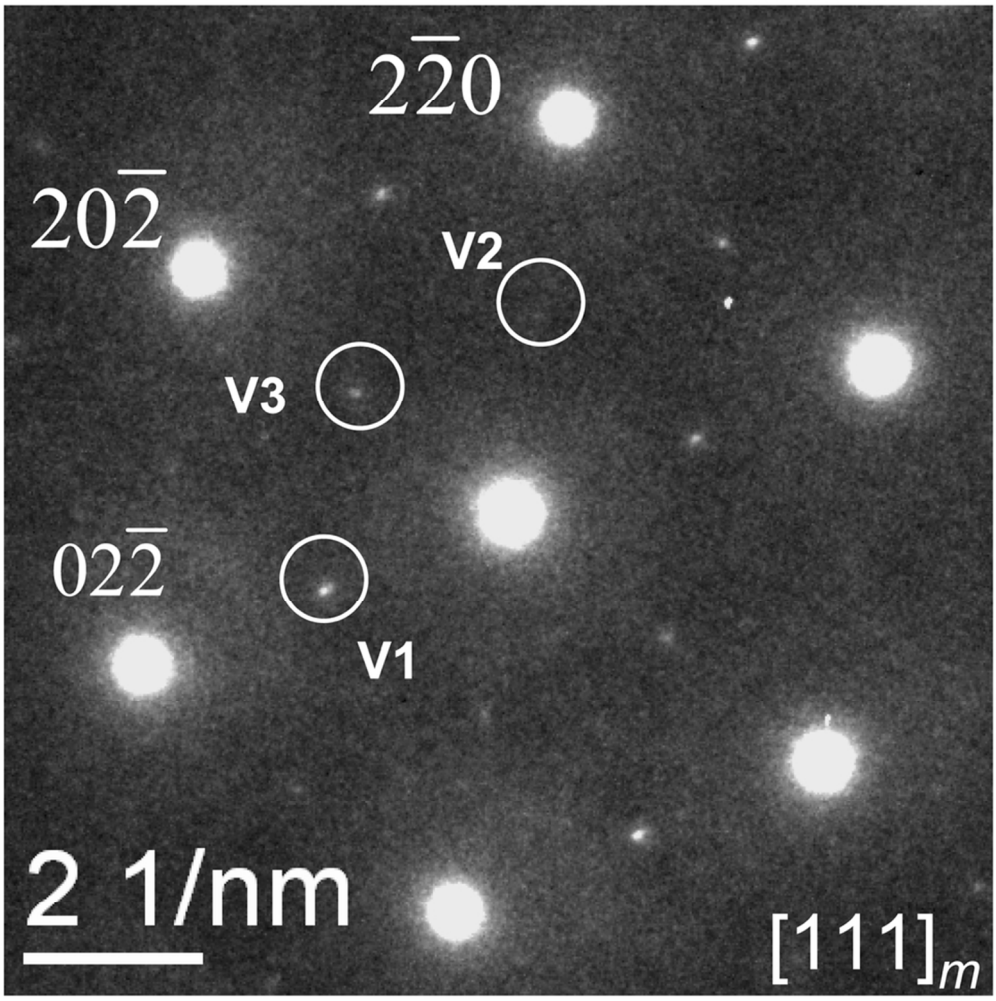

Fig. 4 SAED pattern of $HgIn_2Te_4$. Two variants (V1+V3) were displayed and another variant V2 was not displayed.
82x82mm (300 x 300 DPI)

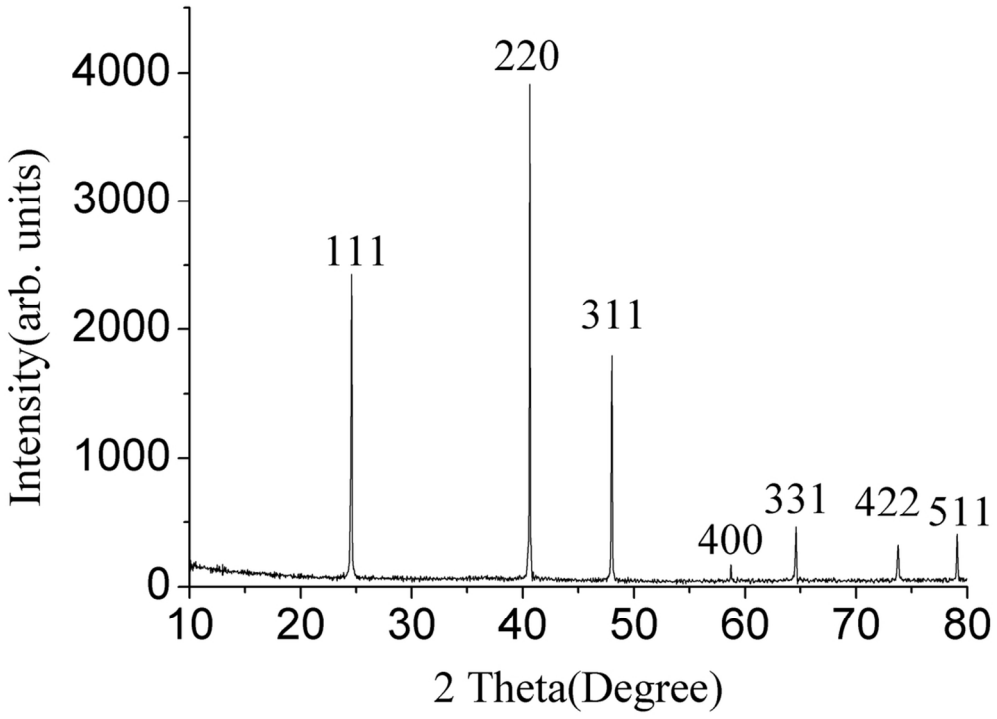

Fig. 5 Typical powder XRD pattern of $Hg_3In_2Te_6$ samples measured at room temperature.
51x37mm (600 x 600 DPI)

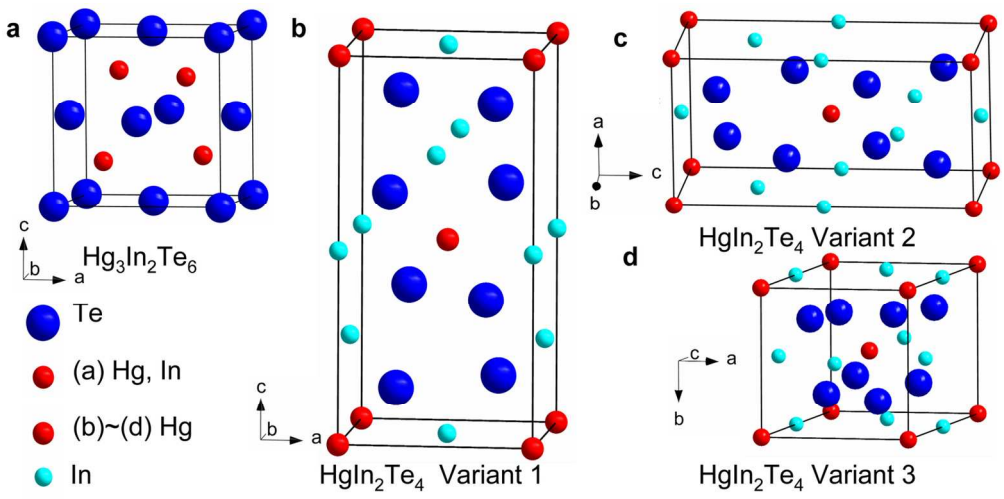

Fig. 6 Orientation relationship between $Hg_3In_2Te_6$ matrix and $HgIn_2Te_4$ variants 1~3: (a) $Hg_3In_2Te_6$ matrix; (b)~(d) $HgIn_2Te_4$ variants 1~3.
70x35mm (600 x 600 DPI)

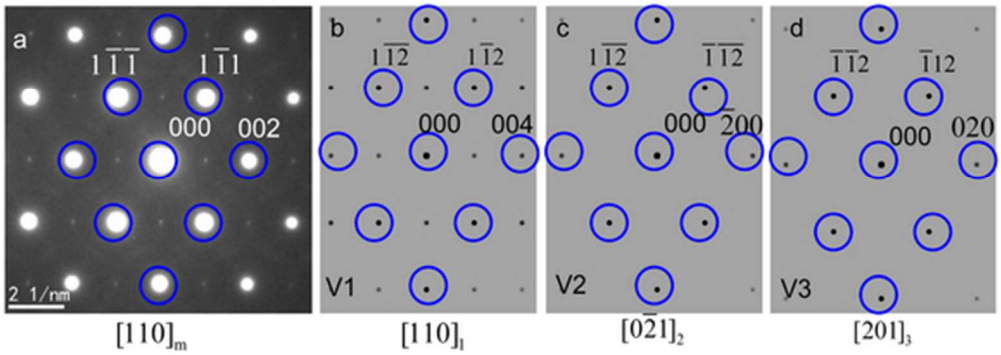

Fig. 7 SAED pattern and simulated electron diffraction patterns of V1~3: (a) SAED pattern along $[110]_m$ zone axis; (b) simulated pattern of V1 along $[110]_1$; (c) simulated pattern of V2 along $[0\text{-}21]_2$; (d) simulated pattern of V3 along $[201]_3$.
49x17mm (300 x 300 DPI)

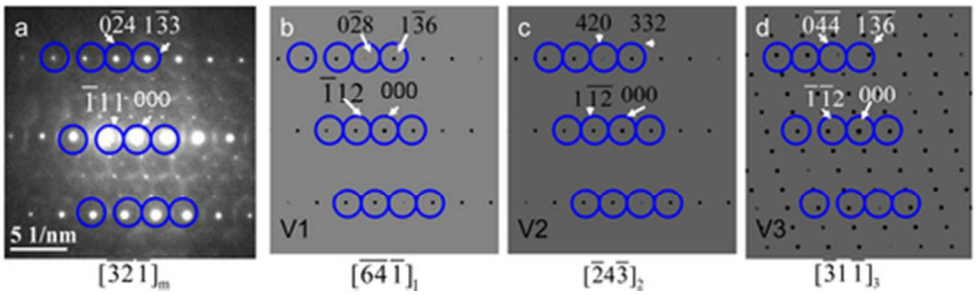

Fig. 8 SAED pattern and simulated electron diffraction patterns of V1~3: (a) SAED pattern along $[-3-2-1]_m$ zone axis; (b) simulated pattern of V1 along $[-6-4-1]_1$; (c) simulated pattern of V2 along $[-24-3]_2$; (d) simulated pattern of V3 along $[-31-1]_3$.
41x12mm (300 x 300 DPI)

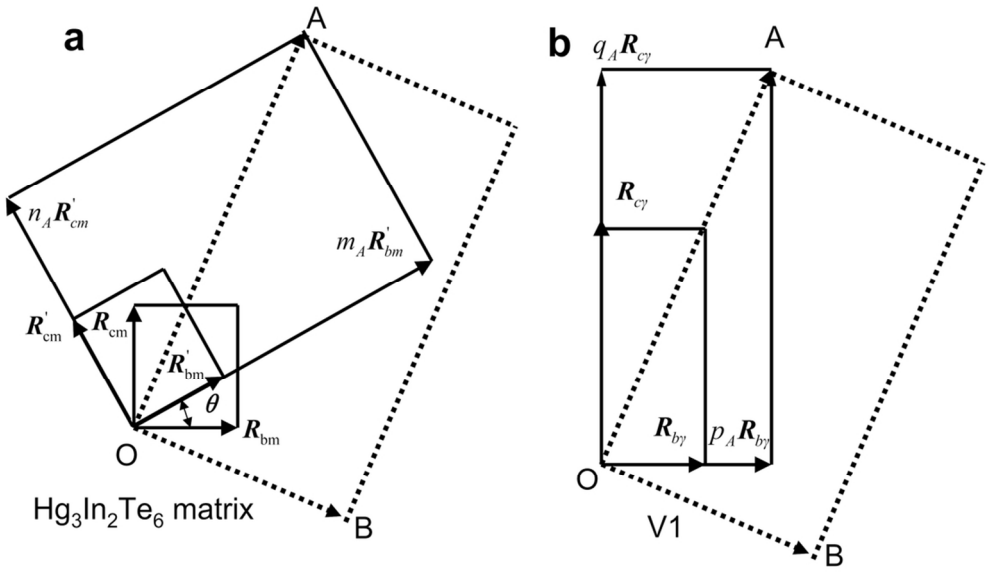

Fig. 9 A coincident site lattice composed of V1 and $Hg_3In_2Te_6$ matrix. ***OA*** and ***OB*** are basic vectors of the coincident site lattice.
49x28mm (600 x 600 DPI)

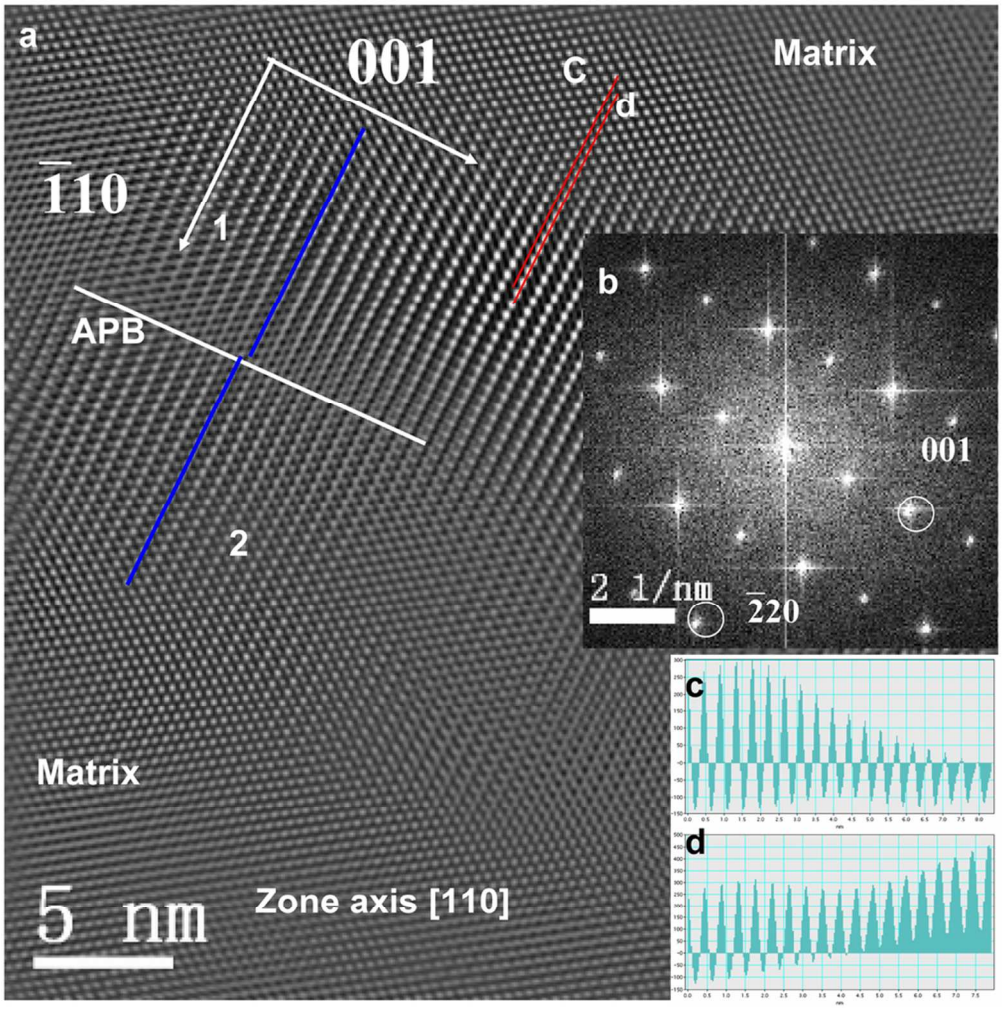

Fig. 10 HRTEM image and the results of $HgIn_2Te_4$ variant 1: (a) HRTEM image; (b) FFT image; (c) and (d) the intensity profiles of the dots along straight lines c and d.
85x85mm (300 x 300 DPI)